

A 3D Level Sets Method for Segmenting the Mouse Spleen and Follicles in Volumetric microCT Images

Jeffery R. Price, Deniz Aykac, and Jonathan Wall

Abstract—We present a semi-automatic, 3D approach for segmenting the mouse spleen, and its interior follicles, in volumetric microCT imagery. Based upon previous 2D level sets work, we develop a fully 3D implementation and provide the corresponding finite difference formulas. We incorporate statistical and proximity weighting schemes to improve segmentation performance. We also note an issue with the original algorithm and propose a solution that proves beneficial in our experiments. Experimental results are provided for artificial and real data.

I. INTRODUCTION

Small animal models have become increasingly important in the study of human disease mechanisms. Mice in particular have received special attention due to extensive homologies between the mouse and human genome and the relative ease of genomic manipulation [1]. Recent improvements in small animal imaging technologies – including CT, SPECT, and PET – have enabled high-resolution *in vivo* anatomic and functional studies. Our work is motivated by multi-modality imaging (SPECT+CT and/or SPECT+PET) for the quantification of amyloid deposits in a transgenic mouse model of AA-amyloidosis [2]. Our current goal is to provide semi-automatic volumetric segmentation of the mouse spleen using contrast-enhanced microCT data. This can be a challenging problem, as evident from the poor contrast in the example image in Fig. 1. An additional goal of our work is to differentiate the (contrast-enhanced) blood pool in the spleen from the interior follicles (which do not contain blood). The segmentation results are to be subsequently used to quantify the amount of amyloid radiotracer in the spleen blood pool and as an attenuation map for SPECT or PET data correction. Furthermore, we expect in the future to analyze the 3D follicular structure inside the spleen and how that structure might be altered under disease and/or treatment scenarios.

A thorough summary of level sets methods for medical imagery applications can be found in [3]. Our efforts in this paper expand upon our work from [4], which was based upon the approach initially set forth by Chan and Vese [5]. In

[4], semi-automatic 3D spleen segmentation was performed using the 2D approach from [5], beginning with a manually-selected seed point near the center of the spleen volume, and proceeding slice-by-slice. We improved segmentation performance using statistical weighting, based on

J. Price and D. Aykac are with the Image Science and Machine Vision Group, Oak Ridge National Laboratory, Oak Ridge, TN, USA. E-mail: {pricejr,aykacdb}@ornl.gov.

J. Wall is with the Graduate School of Medicine, University of Tennessee, Knoxville, TN, USA. E-mail: jwall@ut.utmck.edu.

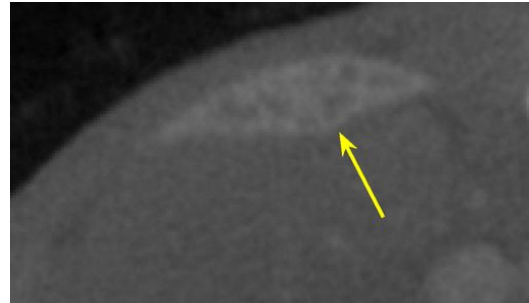


Fig. 1. An example region from a microCT slice. The spleen is indicated with the arrow.

the grayscale characteristics of the previously segmented slice, as well as proximity weighting, based upon the final contour location of the previously segmented slice. In this paper, we extend the approach to a fully 3D implementation, providing the corresponding finite difference formulas, and adapt both the statistical and proximity ideas to the 3D case. We also note an issue with the original algorithm in scenarios where one might wish to weight the desired foreground and background regions differently. We propose a solution to this issue and use the modified algorithm to more effectively segment follicles within the spleen.

The remainder of this paper is organized as follows. In Section II, we review the model proposed in [5] and derive the 3D discretized implementation. We continue in Section III by describing our modifications to the algorithm of Section II. We present experimental results on both artificial and real data in Section IV and close in Section V.

II. MODEL DESCRIPTION

In the segmentation problem, we seek a contour (surface) C such that the region of interest (e.g., the spleen) is inside the contour and the background is outside. In the level set formulation [6], C is defined implicitly as the zero level set of a function $f : \Omega \rightarrow \mathbb{R}$ where $\Omega \subset \mathbb{R}^3$ represents the image domain. The segmentation problem then becomes a search for the optimal $f(\cdot)$. The surface is formally defined as $C = \{(x, y, z) : f(x, y, z) = 0\}$ where we define the region inside the surface, C_+ , by $f(x, y, z) > 0$ and the region outside, C_- , by $f(x, y, z) \leq 0$.

Adopting the construction in [5], the energy functional we

seek to minimize is expressed by

$$\begin{aligned}
J_\epsilon(f) &= \nu \int_{\Omega} \delta_\epsilon(f(x, y, z)) |\nabla f(x, y, z)| dx dy dz \\
&+ \lambda_1 \int_{\Omega} |I(x, y, z) - c_1|^2 H_\epsilon(f(x, y, z)) dx dy dz \\
&+ \lambda_2 \int_{\Omega} |I(x, y, z) - c_2|^2 (1 - H_\epsilon(f(x, y, z))) dx dy dz,
\end{aligned} \tag{1}$$

where

$$c_1 = \frac{\int_{\Omega} I(x, y, z) H_\epsilon(f(x, y, z)) dx dy dz}{\int_{\Omega} H_\epsilon(f(x, y, z)) dx dy dz}, \tag{2}$$

$$c_2 = \frac{\int_{\Omega} I(x, y, z) (1 - H_\epsilon(f(x, y, z))) dx dy dz}{\int_{\Omega} (1 - H_\epsilon(f(x, y, z))) dx dy dz}, \tag{3}$$

$H_\epsilon(\cdot)$ and $\delta_\epsilon(\cdot)$ represent regularized Heaviside step and Dirac delta functions, respectively, and $I(\cdot)$ is the image we seek to segment. The c_1 and c_2 terms are the (regularized) average values of the image inside C (C_+) and outside C (C_-), respectively. Examining Eq. (1), the first term, weighted by the parameter ν , represents the surface area of C and hence controls the smoothness of the resulting surface. The other two terms, weighted by parameters λ_1 and λ_2 , are the image-based terms and represent the variation of the image in C_+ and in C_- , respectively. The benefit to this formulation is that the image-based terms are independent of the image gradient; rather than seeking to align on image edges, the resulting contour seeks to divide the image into two homogeneous regions. This approach is much more robust than gradient-based methods when attempting to segment images with weak edges.

Eq. (1) is minimized via an Euler-Lagrange approach using artificial time, resulting in the following PDE:

$$\frac{\partial f}{\partial t} = \delta_\epsilon(f) \left[\nu \operatorname{div} \left(\frac{\nabla f}{|\nabla f|} \right) - \lambda_1 (I - c_1)^2 + \lambda_2 (I - c_2)^2 \right], \tag{4}$$

where the dependencies on (x, y, z) have been left implicit for notational convenience. To solve this PDE, we apply finite difference schemes in both time and space, where

$$\frac{\partial f}{\partial t} \rightarrow \frac{f^{n+1} - f^n}{\Delta t}, \tag{5}$$

$f(x, y, z) \rightarrow f_{i,j,k}$, and $I(x, y, z) \rightarrow I_{i,j,k}$. We approximate the divergence term using

$$\operatorname{div} \left(\frac{\nabla f}{|\nabla f|} \right) \rightarrow \hat{\Delta}_x f + \hat{\Delta}_y f + \hat{\Delta}_z f \tag{6}$$

where

$$\begin{aligned}
\frac{\partial}{\partial x} \left(\frac{\partial f / \partial x}{|\nabla f|} \right) &\rightarrow \hat{\Delta}_x f = \\
&D_-^x \circ \left(\frac{D_+^x f}{\sqrt{(D_+^x f)^2 + (D_c^y f)^2 + (D_c^z f)^2}} \right) = \\
&\frac{D_+^x f}{\sqrt{(D_+^x f)^2 + (D_c^y f)^2 + (D_c^z f)^2}} - \\
&\frac{D_+^x f_{i-1}}{\sqrt{(D_+^x f_{i-1})^2 + (D_c^y f_{i-1})^2 + (D_c^z f_{i-1})^2}}.
\end{aligned} \tag{7}$$

D_-^x , D_c^x , and D_+^x represent forward, central, and backward difference operators in the x direction (and similarly for y and z). $\hat{\Delta}_y f$ and $\hat{\Delta}_z f$ from Eq. (6) are defined like Eq. (7), where central differencing is used for the other directions in the gradient magnitude approximation (i.e., for $\hat{\Delta}_x f$, central differencing is used for y and z). For notational convenience in Eq. (7), we have left the subscripts on $f_{i,j,k}$ implicit unless changed, as in f_{i-1} in the last term. (Note that $D_+^x f_{i-1} = D_-^x f$, which is used in [5] and [7].)

The resulting iteration for updating the level set function $f(\cdot)$ at each time step can then be expressed

$$\begin{aligned}
f^{n+1} &= f^n + \nu \Delta t (\hat{\Delta}_x f^n + \hat{\Delta}_y f^n + \hat{\Delta}_z f^n) \\
&- \lambda_1 \Delta t (I - c_1)^2 + \lambda_2 \Delta t (I - c_2)^2.
\end{aligned} \tag{8}$$

For the discretizations above, note that we have employed a simple finite difference scheme (based on that in [5]) for Eq. (7) and that the iteration in Eq. (8) is explicit in f^n . Though our experimental results have been satisfactory, some benefits may be gained by employing more robust schemes [8] and/or a semi-implicit approach for the iteration [5], [7].

III. ALGORITHM MODIFICATIONS

Although strikingly effective on many challenging images, the basic algorithm described above has proven ineffective on our spleen data sets (see Section IV for an example). To adapt the method for our use, we previously proposed [4] modifying the image used for segmentation by applying statistical and proximity weighting terms to the original. We adopt a similar approach here, but extend the method to 3D with some minor modifications. For the case of follicle segmentation, we propose a slight modification to the energy functional from Eq. (1), which also results in a change to the iteration of Eq. (8).

A. Spleen Segmentation Step-by-Step

We begin with a manually-selected seed point near the 3D center of the spleen. We define a small sphere around the seed point as the initial surface and initialize the level set function f^0 to the signed distance from this sphere. Define C_+^m to be the interior of the surface at iteration m , where C_+^0 is interior of the seed point sphere, and also define $U_{i,j,k}$ to be the original grayscale image, which does not change

with m . Beginning at $m = 1$, our algorithm for spleen segmentation proceeds as follows.

- 1) Compute the mean μ^{m-1} and standard deviation σ^{m-1} of the voxels in C_+^{m-1} .
- 2) Compute the image $I_{i,j,k}^m$ defined by

$$I_{i,j,k}^m = \frac{1}{\sqrt{|f_{i,j,k}^{m-1}|}} \exp\left(\frac{-(U_{i,j,k} - \mu^{m-1})^2}{2(\sigma^{m-1})^2}\right) \quad (9)$$

and renormalize it to $[0,255]$. Since f^{m-1} is a signed distance function (enforced in Step 5 below), the first term (proximity) penalizes points that are far from the previous contour. The second term (statistical) penalizes points whose gray values are significantly different from those inside the previous contour. The Gaussian distribution used for the statistical term, though not truly representative of the grayscale distribution in the spleen, is nonetheless effective.

- 3) Apply only a few iterations (in n) of the basic level set algorithm from Section II to $I_{i,j,k}^m$ with f^{m-1} as the initialization. Only a few iterations (we use 5) are used to prevent selection of extraneous regions. Call the resultant level set function \hat{f}^m (which may no longer be a signed distance function).
- 4) Find all connected regions where $\hat{f}^m > 0$, keep only the one with the largest volume (again to exclude extraneous regions). This region defines C_+^m .
- 5) If $C_+^m = C_+^{m-1}$, STOP. Otherwise, compute f^m to be the signed distance function corresponding to C_+^m .
- 6) Increment m , return to step 1 above, and repeat.

Due to the interior follicles, the final result often contains many holes. Currently, we take the final C_+ and apply 3D morphological closing to fill all such holes. Since the spleen is a smooth surface, this approach is effective and does not significantly degrade the shape. We are, however, currently experimenting with topology preservation [9] as a potentially better solution.

B. Modified Energy Functional for Follicle Segmentation

In most applications, the parameters λ_1 and λ_2 are set equal to 1.0 and the ν parameter is used to balance the smoothness and image-based terms. In some cases, however, one might wish to weight one region more heavily, implying that $\lambda_1 \neq \lambda_2$. Suppose, without loss of generality, that we are primarily concerned with isolating all bright image regions (e.g., the follicles in inverse gray scale) and desire the surface C to tightly enclose these bright regions (so that $c_1 > c_2$). In this case, we might be tempted to make $\lambda_1 > \lambda_2$. Note, however, that the energy functional from Eq. (1) does not consider the relative values of c_1 and c_2 , only the homogeneity in C_+ and C_- . In fact, the result of using $\lambda_1 > \lambda_2$ is that the C_+ will indeed be brighter on average than the C_- , but the brightest image regions can actually be excluded from C_+ to improve its homogeneity. This is illustrated later in Section IV (see Fig. 6). To address this issue, we propose the following solution.

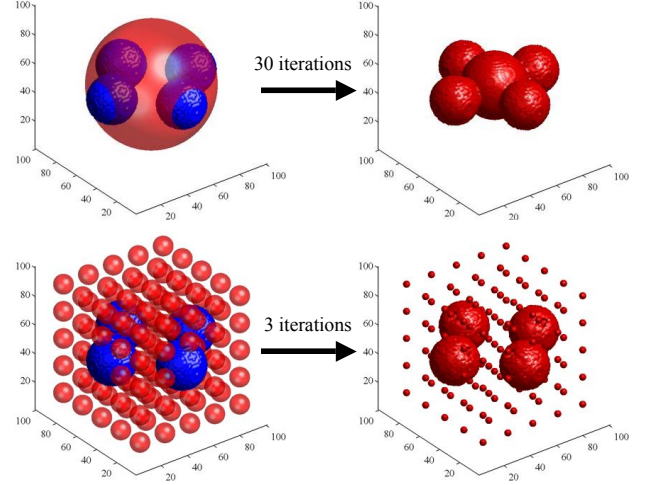


Fig. 2. Segmenting a four-sphere phantom using the basic algorithm from Section II with two different initializations. Initializations are shown on the left (transparent) with the true surface (solid). Progress after the indicated number of iterations is shown on the right. The top initialization converges to the true surface after more than 80 iterations. The bottom initialization converges in only 4 iterations.

Referring back to Eq. (1), we replace Ω in the λ_1 integral term with a new domain Ω_1 defined by

$$\Omega_1 : \{(x, y, z) : I(x, y, z) < c_1\} \quad (10)$$

so that integration is restricted to only the regions where the image is less than c_1 . In other words, we no longer penalize regions that are “too bright.” The resulting change to the iteration in Eq. (8) is

$$\lambda_1 \Delta t (I - c_1)^2 \rightarrow \mathcal{N} \cdot (\lambda_1 \Delta t (I - c_1)^2) \cdot (1 - H(I - c_1)) \quad (11)$$

where $H(\cdot)$ is the Heaviside step function and \mathcal{N} is a normalization term given by $\mathcal{N} = (\int_{\Omega} dx dy dz) / (\int_{\Omega_1} dx dy dz)$ to ensure that the c_1 and c_2 contributions remain consistent. We apply this modification in our results below when segmenting the follicles within the spleen.

IV. RESULTS

In this section we show some experimental results obtained using the algorithms described above.

A. Artificial Data

We begin with an artificial data set of $101 \times 101 \times 101$ voxels containing four spheres of gray value 255 in a background of all 0. We applied the basic 3D algorithm from Section II using two different initializations; the results are illustrated in Fig. 2. We used $\Delta t = 0.025$, $\lambda_1 = \lambda_2 = 1$, and $\nu = 0.001 \times 255^2$ (where 255 is the maximum grayscale value, which is used to balance the contribution from the image-based terms with the smoothness term). The first initialization was a single sphere that intersected all four of the object spheres. The second initialization was a grid of small spheres covering the image domain, similar to the 2D grid initializations used in [7] and [10]. Both

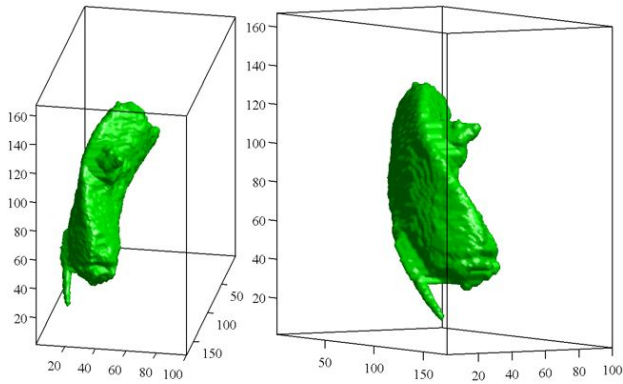


Fig. 3. The result (still not converged after 1000 iterations) of applying the basic algorithm from Section II to our spleen data set. A nearby rib (bottom left) and blood vessel (cone like protrusion) are also captured.

initializations did produce the correct result, but the single sphere initialization took over 80 iterations, while the grid initialization took only 4 iterations. This is consistent with the results presented in [10] and motivates us to use grid-based initialization for follicle segmentation. Recall that our spleen segmentation is seed-point based, hence grid initialization would be inappropriate.

B. Spleen Segmentation

We next tested on a microCT volume of 0.1mm resolution acquired from a mouse injected with 350 μ l of vascular contrast agent to enhance blood pool visibility. CT reconstruction was performed using a fast Feldkamp reconstruction [11]. An example reconstructed slice from this data set was shown earlier in Fig. 1. We processed a sub-volume of 174 \times 100 \times 167 voxels that completely enclosed the spleen. This sub-volume was extracted from the original data set of 512 \times 512 \times 768. Recall that the segmentation is seed-point based; hence, sub-volume processing does not indicate a limitation. In fact, we could begin with a smaller sub-volume and allow it to grow with the segmentation.

We first applied the basic algorithm from Section II using $\Delta t = 0.1$, $\lambda_1 = \lambda_2 = 1$, and $\nu = 0.005 \times 255^2$. We stopped the processing after 1000 iterations (convergence still not achieved) and kept only the largest volume connected region (as in Step 4 of our algorithm). The resulting surface is shown in Fig. 3. Not all of the spleen is captured and other nearby structures (bones and blood vessels) are also captured.

We next applied our modified algorithm from Section III-A with parameters $\Delta t = 0.05$, $\lambda_1 = \lambda_2 = 1$, and $\nu = 0.005 \times 255^2$. For each application of the inner level set algorithm (Step 3), only 5 iterations were used. Convergence was achieved after 6 iterations of the process and the result is illustrated in Fig. 4.

C. Follicle Segmentation

Here we seek to isolate the low contrast follicle regions within the spleen. We take the final result from our spleen segmentation to denote the appropriate region of interest and use grid initialization within this region. We invert

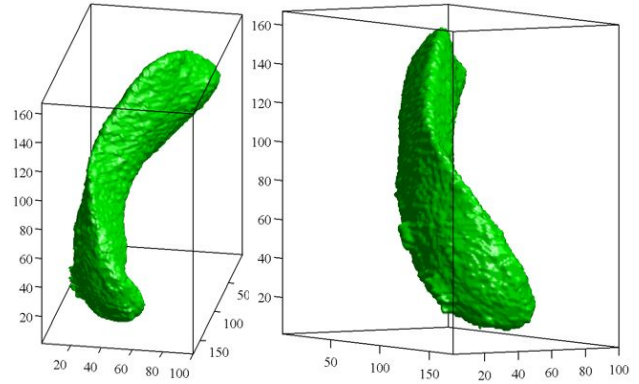


Fig. 4. Resulting spleen surface from our algorithm of Section III-A. Viewpoints are the same as those in Fig. 3.

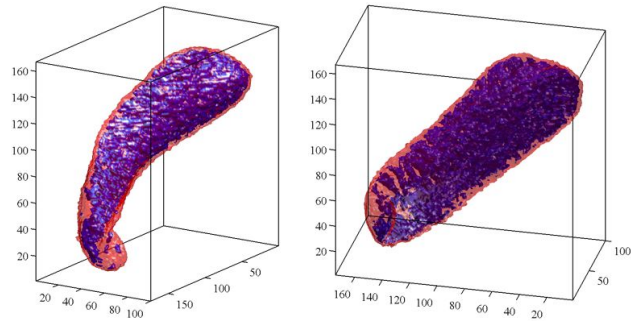


Fig. 5. Follicles (inside transparent spleen) resulting from $\lambda_1 = \lambda_2 = 1$. The segmentation is not tight enough, resulting in follicle regions that are too large.

the grayscale values so that the follicles are bright, and renormalize to [0,255] based only upon the grayscale values inside the spleen. We first apply the basic algorithm from Section II with $\Delta t = 0.05$, $\nu = 0.001 \times 255^2$, and $\lambda_1 = \lambda_2 = 1$. The resulting surface is shown in Fig. 5. The segmentation in this case is not tight enough and the follicle regions are too large.

In an attempt to make the segmentation tighter around the follicles, we reapplied the basic algorithm with $\lambda_1 = 1.5$. We show a slice from the result in Fig. 6; note how homogeneity is the driving factor and regions that are quite bright are excluded. Finally, we applied our modified algorithm from Section III-B using $\lambda_1 = 15$. The result is illustrated in Fig. 7.

V. CONCLUSIONS AND FUTURE WORK

In this paper, we have developed a 3D semi-automatic approach for segmenting the mouse spleen, and its interior follicles, in volumetric microCT imagery. We extended our earlier approach, incorporating statistical and proximity weighting, to a fully 3D implementation and provided the corresponding finite difference formulas. We also noted an issue with the original algorithm in the presence of unequal image-based weighting and subsequently proposed a solution that proved helpful in segmenting the follicles.

In ongoing efforts, we plan to explore the performance of the statistical weighting in 3D vs. 2D. In the 2D slice-to-slice

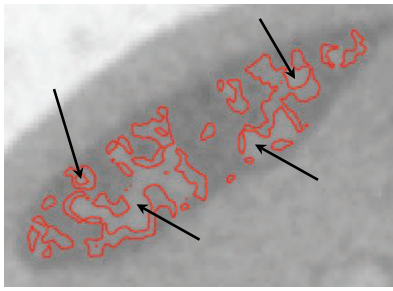


Fig. 6. An example slice from follicle segmentation (inverted grayscale) using the basic algorithm (Section II) with $\lambda_1 = 1.5$ and $\lambda_2 = 1$. Regions that are “too bright” are excluded (examples indicated with arrows).

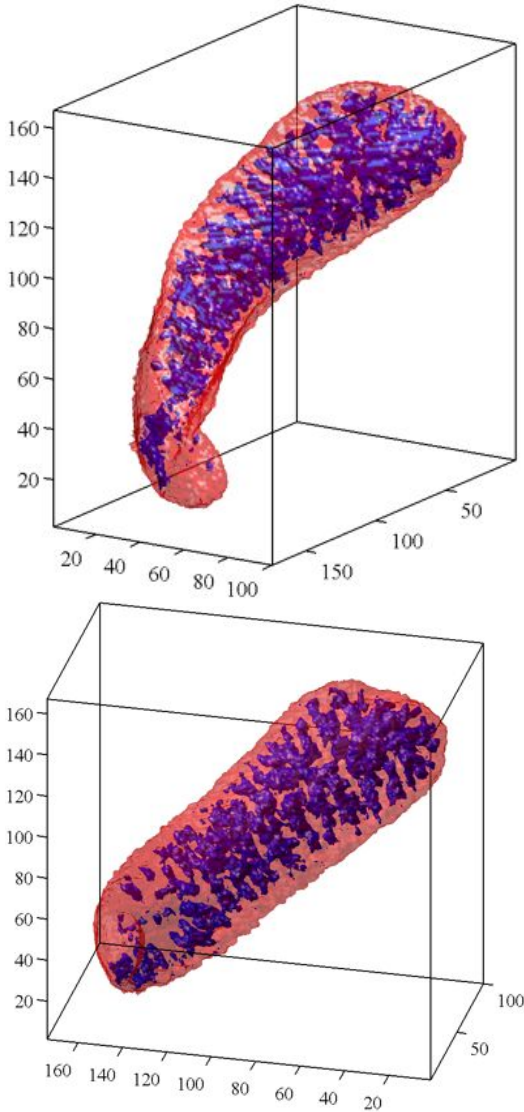


Fig. 7. Follicles (inside transparent spleen) found using the proposed approach described in Section III-B with $\lambda_1 = 15$ and $\lambda_2 = 1$. Viewpoints are the same as those in Fig. 5.

approach of our previous work, the statistics are update based only upon the adjacent slice and can hence track contrast variation along the z axis. We plan to implement and evaluate a spatially adaptive statistical weighting scheme to achieve

this in 3D. We will also determine if replacing the normal distribution from Eq. (9) with a more accurate parametric distribution is helpful, perhaps incorporating maximum likelihood measures into the energy functional as in [12]. Finally, we are in the process of applying topology preservation [9] in our algorithm to determine its efficacy in our work.

ACKNOWLEDGMENTS

This work was supported by USPHS Research Grant EB000789 from the National Institute of Biomedical Imaging and Bioengineering and the National Institute of Neurological Disorders and Stroke. Prepared by Oak Ridge National Laboratory, managed by UT-Battelle, LLC, for the U.S. Department of Energy under Contract No. DE-AC05-00OR22725.

REFERENCES

- [1] National Human Genome Research Institute. Background on mouse as a model organism. [Online]. Available: <http://www.genome.gov/10005834>
- [2] J. Wall, S. Kennel, M. Paulus, S. Gleason, J. Gregor, J. Baba, M. Schell, T. Richey, B. O’Nuallain, R. Donnell, P. Hawkins, D. Weiss, and A. Solomon, “Quantitative high-resolution microradiographic imaging of amyloid deposits in a novel murine model of AA-amyloidosis,” *Amyloid*, vol. 12, no. 3, pp. 149–156, 2005.
- [3] J. Suri, K. Liu, S. Singh, S. Laxminarayan, X. Zeng, and L. Reden, “Shape recovery algorithms using level sets in 2-D/3-D medical imagery: a state-of-the-art review,” *IEEE Transactions on Information Technology in Biomedicine*, vol. 6, no. 1, pp. 8–28, 2002.
- [4] D. Aykac, J. Price, and J. Wall, “3D segmentation of the mouse spleen in microCT via active contours,” in *Proceedings of the IEEE Nuclear Science Symposium and Medical Imaging Conference*, vol. 3, 2005, pp. 1542–1545.
- [5] T. Chan and L. Vese, “Active contours without edges,” *IEEE Transactions on Image Processing*, vol. 10, no. 2, pp. 266–277, 2001.
- [6] S. Osher and J. Sethian, “Fronts propagating with curvature-dependent speed: algorithms based on Hamilton-Jacobi formulation,” *Journal of Computational Physics*, vol. 79, pp. 12–49, 1988.
- [7] L. Vese and T. Chan, “A multiphase level set framework for image segmentation using the Mumford and Shah model,” University of California, Los Angeles, UCLA CAM Report 01-25, 2001.
- [8] H.-K. Zhao, T. Chan, B. Merriman, and S. Osher, “A variational level set approach to multiphase motion,” *Journal of Computational Physics*, vol. 127, pp. 179–195, 1996.
- [9] X. Han, C. Xu, and J. L. Prince, “A topology preserving level set method for geometric deformable models,” *IEEE Transactions on Pattern Analysis and Machine Intelligence*, vol. 25, no. 6, pp. 755–768, 2003.
- [10] B. Sumengen and B. Manjunath, “Graph partitioning active contours (GPAC) for image segmentation,” *IEEE Transactions on Pattern Analysis and Machine Intelligence*, vol. 28, no. 4, pp. 509–521, 2006.
- [11] J. Gregor, S. Gleason, M. Paulus, and J. Cates, “Fast Feldkamp reconstruction based on focus of attention and distributed computing,” *International Journal for Imaging Systems and Technology*, vol. 12, no. 229-234, 2002.
- [12] A. Sarti, C. Corsi, E. Mazzini, and C. Lamberti, “Maximum likelihood segmentation of ultrasound images with rayleigh distribution,” *IEEE Transactions on Ultrasonics, Ferroelectrics, and Frequency Control*, vol. 52, no. 6, pp. 947–960, 2005.